

Delbrück scattering at energies $140 \div 450$ MeV.

SH.ZH. AKHMADALIEV, G.YA. KEZERASHVILI, S.G. KLIMENKO, V.M. MALYSHEV,
A.L. MASLENNIKOV, A.M. MILOV, A.I. MILSTEIN, N.YU. MUCHNOI,
A.I. NAUMENKOV, V.S. PANIN, S.V. PELEGANCHUK, V.G. POPOV,
G.E. POSPELOV, I.YA. PROTOPOPOV, L.V. ROMANOV, A.G. SHAMOV,
D.N. SHATILOV, E.A. SIMONOV, YU.A. TIKHONOV
Budker Institute of Nuclear Physics, 630090 Novosibirsk, Russia

The differential cross section of Delbrück scattering is measured on a bismuth germanate ($\text{Bi}_4\text{Ge}_3\text{O}_{12}$) target at photon energies $140 \div 450$ MeV and scattering angles $2.6 \div 16.6$ mrad. A good agreement with the theoretical results, obtained exactly in a Coulomb field, is found.

I. INTRODUCTION

Delbrück scattering [1] is a process, in which the initial photon turns into a virtual electron-positron pair, it is scattered in a Coulomb field of a nucleus and then transforms into the final photon (Fig. 1a). Thus, the final photon energy is equal to the energy of the initial photon (elastic scattering).

The interest to the experimental study of Delbrück scattering has the following motivations. First, it is one of nonlinear quantum electrodynamic processes accessible at present time to direct observation. Other such process is photon splitting in a Coulomb field (Fig. 1b). For these processes the contribution of higher orders of the perturbation theory with respect to the parameter $Z\alpha$ ($Z|e|$ is the charge of the nucleus, $\alpha = e^2 = 1/137$ is the fine-structure constant, e is the electron charge, $\hbar = c = 1$) at large Z essentially modifies the cross section. Therefore, the investigation of these processes can be used as a good test of quantum electrodynamics in a strong electromagnetic field. Second, Delbrück scattering is a background process to the nuclear Compton scattering, which is an effective experimental tool to study mesonic and nucleon internal degrees of freedom of nucleus [2].

At present, four methods of Delbrück scattering amplitude calculation are used, possessing different areas of applicability :

I) The amplitude is calculated in the lowest in $Z\alpha$ order of the perturbation theory, but for an arbitrary photon energy ω and scattering angle θ . The review of numerous results, obtained in this approximation, can be found in [3,4]. These results are applicable only at small Z , when the parameter $Z\alpha \ll 1$.

II) At high photon energies $\omega \gg m$ (m is the electron mass) and small scattering angles $\theta \ll 1$ the amplitude is obtained by summing in a definite approximation of the Feynman diagrams with an arbitrary number of photons exchanged with a Coulomb centre [5].

III) At $\omega \gg m$ and $\theta \ll 1$ it is possible to use also a quasiclassical approach [6], since in this case the momentum transfer $\Delta = |\mathbf{k}_2 - \mathbf{k}_1| = \omega\theta$ (\mathbf{k}_1 and \mathbf{k}_2 being the momenta of the initial and final photons, re-

spectively), and the characteristic angular momentum $l \sim \omega/\Delta = 1/\theta \gg 1$. Numerically, the approaches II and III lead to the same results, as they should, and show the significant difference between the cross section calculated exactly in $Z\alpha$ and the cross section obtained in the lowest order of the perturbation theory.

IV) At $\omega \gg m$ and $\theta \sim 1$ the amplitude is calculated exactly in $Z\alpha$ but neglecting the electron mass as compared to ω and Δ [7,8]. The approach is based on the use of the relativistic electron Green function in a Coulomb field. In this case the Coulomb effects are also significant.

The numerical results for the Delbrück scattering amplitudes obtained with the use of all four methods at different ω , θ and Z can be found in ref. [9]. In our work we use the results obtained by method III, which is applicable under conditions of our experiment.

In the experimental investigations of Delbrück scattering carried out earlier, three different photon sources have been used :

1) Photons from radioactive sources, for instance ^{24}Mg ($\omega = 2.75$ MeV) [10,11].

2) Photons from nuclear reactions like capture of thermal neutrons in the energy range $\omega = 4 \div 12$ MeV [12,13].

3) In the energy range $20 \div 100$ MeV the experiment has been carried out with tagged bremsstrahlung photons [14]. In experiment [15] Delbrück scattering above 1 GeV has been investigated using bremsstrahlung photons without tagging.

The accuracy of photon scattering cross section measurements in the experiments [10–13] allowed one not only to observe Delbrück scattering, but to establish the importance of the Coulomb corrections to the cross section as well. Unfortunately, in this energy range ($\omega \sim m$) the Coulomb corrections are not calculated up to now, that does not permit to perform the detailed comparison between experiment and theory.

At $\omega \gg m$ the amplitudes of Delbrück scattering are calculated including Coulomb corrections. However, the accuracy of cross section measurements achieved in experiments [14–15] is essentially smaller than the accuracy of the theoretical predictions.

In the present experiment tagged backscattered Compton photons of energies $140 \div 450$ MeV were used. The

final photons were detected at scattering angles $2.6 \div 16.6$ mrad. At the specified parameters the theoretical predictions based on the quasiclassical approach (method III) have high accuracy, errors of the calculation less than one percent. At the same time the experimental technique used has allowed us to get high accuracy of cross section measurements and, as a result, to make detailed comparison between theory and experiment.

Apart from Delbrück scattering, we have investigated the process of photon splitting, which has been observed for the first time. Data analysis and comparison with the accurate theoretical predictions for this process are in progress now, preliminary results can be found in [16]. Here we only note that the experimental data within the experimental accuracy ($\sim 10\%$) are in agreement with the results of recent theoretical calculations performed exactly in $Z\alpha$ [17].

II. EXPERIMENTAL SETUP

The experiment has been carried out using ROKK-1M facility [18] of VEPP-4M collider [19]. The experimental setup is shown in Fig. 2. It includes the solid-state laser, optical system of laser beam injection to the vacuum chamber of collider, and photon tagging system [20] of the detector KEDR [21].

High energy photons are produced as a result of laser photons backward Compton scattering on the electron beam. Scattered photons move along the electron beam and have a narrow angular spread of the order $1/\gamma$, where γ is the electron relativistic factor. The photon energy spectrum has a sharp edge with the maximum energy, determined by the following expression :

$$E_{max} = \frac{4\omega_L\gamma^2}{1 + 4\omega_L\gamma/mc^2},$$

where ω_L is the laser photon energy (1.17 eV). The energy of electron beam in experiment was 5.25 GeV, and $E_{max} = 451$ MeV.

Scattered electron is removed from the beam by bending magnets of accelerator and falls on the drift tubes hodoscope of the tagging system. The tagging system allows one to measure the energy of scattered photon with the accuracy about 1.3%. The minimum energy of tagged photons in the experiment was 140 MeV.

The clean photon beam of small cross sizes is formed by the system of three collimators. The first lead collimator has the 10 cm thickness, 4×4 mm² aperture, and it actually sets the cross sizes of the beam. Charged particles of beam halo after this collimator are removed by a sweeping magnet with the magnetic field of 550 G. The second lead collimator, having the 30 cm thickness and 25 mm the diameter of a hole, is placed at 13 m from the first one. It absorbs secondary particles scattered on

large angles. Behind this collimator the third active collimator is placed. It is formed by four BGO crystals of the cross sizes of 25×25 mm² and 150 mm length. An aperture of this collimator (9×9 mm²) was chosen so that its inner edges could not see the interaction point of the laser photon beam and electron beam. Scintillation light from each BGO crystal of this collimator is detected by the photomultiplier, which signal is included in the trigger of the experiment in anticoincidence. The active collimator removes the impurity of secondary particles moving in small angles with respect to the main photon beam.

The target is placed directly behind the last collimator. It is BGO crystal of 12 mm thickness (1.07 radiation length) and 25×25 mm² cross sizes. Light from the crystal is detected by two photomultipliers, which signals are included in a trigger in anticoincidence. It enables us to suppress effectively a background from inelastic processes in the target at the trigger level. The threshold for the energy deposition in the target was set at the level of 150 KeV.

In order to reduce a background from Compton scattering after the target, photons pass the distance between the target and particle detector (4.8 m) in helium-filled tube of 30 cm diameter. The photon passed target without interaction falls onto an absorber installed before the aperture window of the detector. The absorber is the BGO crystal cylinder of 23 mm diameter and 146 mm length. Its signal is also included in a trigger in anticoincidence. It permits one to exclude the trigger start up from the photons, passed target without interaction. To suppress the trigger start up from the charged particles, a thin scintillation veto-counter is mounted on the aperture window of the detector.

The signals from the BGO-collimator, target, absorber, and veto-counter are digitized and used in off-line analysis for background suppression. Besides, the signals from the target and absorber are used to monitor the input gamma flux. The typical rate of the initial photons in experiment was 5 – 10 kHz. These signals are exploited also to form an additional trigger to start the readout of the tagging system for measurement of the energy spectrum of initial photons (Fig.3).

Final photons are detected by means of the electromagnetic calorimeter based on liquid krypton [22]. The layout of the calorimeter is shown in Fig. 4.

The electrodes are made of G10 sheets covered with a copper foil on the both sides. The first (counting from the input window of the calorimeter) and all the odd electrodes are under zero potential ("grounded" electrodes), high voltage is applied to all the even electrodes.

The high-voltage electrodes are used for energy measurements. They are divided into the 9 pads centered around the beam axis. In the longitudinal direction the electrode system is segmented into three sections, altogether the calorimeter contains 27 cells for energy measurements.

The "grounded" electrodes, from second to fourth, are used for the coordinate measurements. Strips are present on the both sides of these electrodes and oriented perpendicularly one to another. It enables us to measure both transverse coordinates (X and Y) in one layer. The strip width varies from 1 cm in the centre to 3 cm on the edge of the calorimeter's aperture. The structure of high-voltage and coordinate electrodes is shown in details in Fig. 5. For such coordinate structure of the calorimeter, the space resolution is equal to 1 mm in the centre and 2.3 mm on the edge.

The high energy resolution of the calorimeter ($2.4\%/\sqrt{E(\text{GeV})}$) and photon tagging allow to use effectively the equality of the initial and final photon energies in Delbrück scattering in order to suppress the background from inelastic processes.

On the initial step of the off-line analysis we select the events (named below as events with a detected photon) satisfying the following criteria:

- 1) One track in the tagging system is found.
- 2) Energy deposition in the crystals of the BGO-collimator and in the absorber is less than 0.35 MeV.
- 3) Energy deposition in the target is less than 0.15 MeV.
- 4) Energy deposition in the scintillation counter on the aperture window of the calorimeter is less than 0.4 MeV.
- 5) Energy deposition in the central tower of the first layer of the calorimeter is more than 80 MeV.
- 6) One photon in the calorimeter is detected.

In Fig. 6 the example of the event with the detected photon is shown. In this event photon conversion has happened in the first X-layer.

The efficiency of photon detection in the calorimeter is about 70% and weakly depends on the photon energy at $\omega > 140$ MeV (Fig. 7). Experimental data shown in Fig. 7 were obtained in runs when the target and absorber were removed. It is seen from this picture that the experimental efficiency is slightly higher than in the simulation. Therefore, in the comparison between the simulation and experiment this difference was taken into account.

III. BACKGROUND PROCESSES FOR DELBRÜCK SCATTERING

The total cross section of Delbrück scattering at $\omega \gg m$ is independent of the photon energy, and the main contribution to it comes from scattering angles $\theta \sim m/\omega$. In the experiment the photons with the scattering angles $2.6 \div 16.6$ mrad were detected. For bismuth ($Z=83$) the visible cross section of Delbrück scattering in this range of angles is equal to 5.9 mb at $\omega = 140$ MeV and 1.2 mb at $\omega = 450$ MeV. For comparison, the total cross section for bismuth equals 6.4 mb. The contribution to the

visible cross section from the scattering on germanium ($Z=32$) is about 3%.

Compton scattering on atomic electrons is the main background process under conditions of our experiment. Its cross section for a bismuth is about 5.3 mb and 4.9 mb at $\omega = 140$ MeV and 450 MeV, respectively. The results of calculations for differential cross sections of Delbrück and Compton scattering on bismuth are shown in Fig. 8.

Secondary photons from showers, arising in target and air, give very small contribution to the background. The low level of this background is the result of the following: the target in the experiment was "active", and the balance between the energy deposition in the calorimeter and the energy of the initial photon was required.

As simulation shows, there is also a small contribution to the background from photons passed the target and the absorber without interaction and, in consequence of shower fluctuations in the calorimeter, detected at $\theta > 2.6$ mrad. The simulation was made with the use of GEANT package (version 3.21).

Besides of Compton scattering and electromagnetic cascades (processes, included in GEANT), photon splitting was also taken into account as a background process. Since the cross section of this process is small in comparison with the cross section of the investigated effect, the approximate formula (the accuracy $\sim 20\%$) based on the Weizsäcker-Williams method was used for the calculation.

Another processes, such as Compton scattering on nuclei, π^0 photoproduction, pair production with radiation of a photon, have been estimated under the conditions of the experiment. The first two processes give negligible contribution to the number of scattered photons detected, while the contribution from the third one is about 0.5%.

Special attention was paid to the background, which comes from Compton and Delbrück scattering on the edges of the last BGO-collimator. This question is discussed in Section IV.

IV. EXPERIMENTAL RESULTS AND CONCLUSION

In order to understand the situation with background, data has been taken in two modes: with target and without target ($9 \cdot 10^8$ and $2 \cdot 10^8$ photons, respectively).

In Fig. 9a-d the two-dimensional distributions of energy deposition E_C in the calorimeter versus initial photon energy E_{TS} for these modes are shown. The events with detected photon having the scattering angle in the range $2.6 \div 16.6$ mrad are selected.

The diagonal band in Fig. 9 a,c corresponds to elastic scattering. In simulation (Fig. 9c) this band contains the events of Compton scattering and events, in which

the initial photon passed the target and absorber without interaction and was detected in the given range of angles. The contribution to this band from showers in the target and air is very small. In the experimental distribution (Fig. 9a) this band is enhanced by virtue of Delbrück scattering in the target.

It is seen from Fig. 9 that in the experiment there is a large number of "inelastic scattering" events, i. e. events with the energy deposition in the calorimeter essentially smaller than the energy of the initial photon. These events are the result of electromagnetic showers generated in the BGO-collimator by the initial photons touched it. Since this effect strongly depends on a position and orientation of the collimator with respect to the axis of the photon beam, it is not possible to simulate this effect accurately. Nevertheless, to subtract this background, one can use the experimental data of empty-target runs. In order to find the correct method of such subtraction, the simulation for empty-target runs was made. In the simulation the BGO-collimator was shifted with respect to the axis of the initial photon beam so that 0.2% of photons touched it, and the signal from the collimator was not taken into account.

Fig. 10 shows the distribution over the parameter $(E_C - E_{TS})/\sigma_c$ (where σ_c is the energy resolution of the calorimeter) obtained as a result of such simulation. One can see that the contribution to the elastic scattering of secondary photons from showers (generated in the BGO-collimator mainly), when $\Delta E = |E_C - E_{TS}| < 2.5\sigma_c$, is rather small. The small difference between simulation and experiment at $\Delta E < 2.5\sigma_c$ can be explained by the fact that Compton scattering in the BGO-collimator can not be simulated correctly, and Delbrück scattering in the collimator was not included in simulation in this case.

Thus, the background from the BGO-collimator for runs with target can be obtained as a difference between experiment and simulation for empty-target runs multiplied by the probability for photon to pass target without interaction. This suppression factor is equal approximately to 0.5 and weakly depends on the energy at $\omega = 140 \div 450$ MeV. This is correct at $\Delta E < 2.5\sigma_c$, while for events with $\Delta E > 2.5\sigma_c$, coming mainly from secondary photons, the suppression factor is bigger due to the charged component of the shower. It is illus-

trated by Fig. 11, which shows, for runs with the target, the distribution of scattered photons over the parameter $(E_C - E_{TS})/\sigma_c$ with taking this background into account.

In Table I we make the comparison between the experiment and the simulation for different energy ranges of initial photon. The results of simulation for Delbrück scattering and the background processes are shown also. Errors in this Table include statistical errors as well as the total systematic error. The latter one includes the error of measurement of the initial photons intensity and the error of photon detection efficiency (see Fig. 6). These errors are estimated to be 1.5% and 1%, respectively.

The differential cross section of Delbrück scattering for unpolarized photons is given by [4]

$$\frac{d\sigma}{d\Omega} = (Z\alpha)^4 r_0^2 \{|A^{++}|^2 + |A^{+-}|^2\},$$

where r_0 is the classical electron radius, A^{++} and A^{+-} are non-helicity-flip and helicity-flip amplitudes.

At $\omega \gg m$ and $\Delta \sim m$, as it was in the experiment, the helicity amplitudes have the form $A \sim \omega f(\Delta)$. Since $d\sigma/d\Omega$ is independent of azimuth angle φ , the differential cross section $d\sigma/dt$ is equal to $(\pi/\omega^2)d\sigma/d\Omega$ (where $t = \Delta^2$) and depends on the momentum transfer Δ , but not on the photon energy ω . It allows one to get the distribution $d\sigma/dt$ with the use of data for all energies of the initial photon (Table. II and Fig. 12).

It is seen from the Table II and Fig.12, that the experimental results are in a good agreement with the theoretical predictions within the experimental accuracy.

ACKNOWLEDGMENTS

We express our gratitude to A.N. Skrinsky and V.A. Sidorov for their interest and support of the present research. We are grateful to V.P. Smakhtin for helpful suggestions, and V.N. Baier, A.E. Bondar, A.P. Onuchin for useful discussion. We also thank the experimental staff of the storage ring VEPP-4M and technical group of the ROKK-1M facility for providing high-quality photon beam. Partial support by Russian Foundation for Basic Research (grant RFBR-97-02-18556) is also gratefully acknowledged.

-
- [1] L. Meitner, H. Kösters (and M. Delbrück), Z.Phys. **84**, 137 (1933).
 - [2] A. Baumann, P. Rullhusen, K. W. Rose *et al.*, Nucl. Phys. **A536**, 87 (1992).
 - [3] P. Papatzacos and K. Mork, Phys. Rep. **21**, 81 (1975).
 - [4] A. I. Milstein and M. Schumacher, Phys. Rep. **243**, 184 (1994).
 - [5] M. Cheng and T. T. Wu, Phys. Rev. **182**, 1873 (1969); Phys. Rev. **D2**, 2444 (1970); Phys. Rev. **D5**, 3077 (1972).

- [6] A. I. Milstein and V. M. Strakhovenko, Phys. Lett. **A95**, 135 (1983); Sov. Phys. JETP **58**, 8 (1983).
- [7] A. I. Milstein and R. Zh. Shaisultanov, J.Phys. **A21**, 2941 (1988).
- [8] A. I. Milstein, P. Rullhusen and M. Schumacher, Phys. Lett. **B247**, 481 (1990).
- [9] H. Falkenberg, A. Hüniger, P. Rullhusen *et al.*, Atomic Data and Nucl. Data Tables **50**, 1 (1992).
- [10] P. Rullhusen, F. Smend, M. Schumacher *et al.*, Z. Physik **A293**, 287 (1979).
- [11] B. Kasten, D. Schaupp, P. Rullhusen *et al.*, Phys. Rev. **C33**, 1606 (1986).
- [12] U. Zurmühl, P. Rullhusen, F. Smend *et al.*, Phys. Lett. **B114**, 99 (1982).
- [13] U. Zurmühl, P. Rullhusen, F. Smend *et al.*, Z. Phys. **A314**, 171 (1983).
- [14] A. Baumann, P. Rullhusen, K. W. Rose *et al.*, Nucl. Phys. **A536**, 87 (1992).
- [15] G. Jarlskog, L. Jönsson, S. Prünster *et al.*, Phys. Rev. **D8**, 3813 (1973).
- [16] Sh. Zh. Akhmadaliev, G. Ya. Kezerashvili, V. A. Kiselev *et al.*, PHOTON'97, Incorporating the XIth International Workshop on Gamma-Gamma Collisions, Egmond aan Zee, Netherlands, 246 (10-15/05/97).
- [17] R. N. Lee, A. I. Milstein, and V. M. Strakhovenko, JETP **85**, 1049 (1997); Phys. Rev. **A57**, 2325 (1998).
- [18] G. Ya. Kezerashvili, A. M. Milov, N. Yu. Muchnoi *et al.*, AIP Conference Proceedings **343**, 260. (American Institute of Physics, Woodbury, New York, 1995).
- [19] I. Ya. Protopopov, Proceedings of XIII International conference on high energy accelerators of charged particles, **1**, 63, Novosibirsk (1987).
- [20] V. M. Aulchenko, B. O. Baibusinov, S. E. Baru *et al.*, NIM **A355**, 261 (1995).
- [21] V. V. Anashin, V. M. Aulchenko, B. O. Baibusinov *et al.*, Proceedings of International Symposium on Position Detectors in High Energy Physics, 58, Dubna (1988).
- [22] V. M. Aulchenko, A. E. Bondar, P. Cantoni *et al.*, NIM **A394**, 35 (1997).

Figure captions

Fig. 1. (a) Feynman diagrams for Delbrück scattering: the Furry representation and the representation via the usual diagrams of the perturbation theory. The double line denotes the electron Green function in the Coulomb field, crosses denote the Coulomb field. (b) Feynman diagrams in the Furry representation for photon splitting.

Fig. 2. The experimental setup.

Fig. 3. Energy spectrum of the incoming tagged photons.

Fig. 4. Layout of the calorimeter: external vessel (1), copper shield (2), internal vessel (3), signal cable (4), veto-electrode (5), strip electrodes (6), towers (L1, L2, L3).

Fig. 5. Electrode structure of the calorimeter.

Fig. 6. The energy deposition on the strips for the event with the detected photon (the reconstructed coordinates are $X=1.46$ cm, $Y=-2.56$ cm).

Fig. 7. The efficiency of photon detection: experiment (circles), simulation (line).

Fig. 8. The differential cross section for Delbrück (solid lines) and Compton (dashed lines) scattering on bismuth.

Fig. 9. Distributions of energy deposition E_C in the calorimeter versus the initial photon energy E_{TS} for events with the detected photons having scattering angles in the range $2.6 \div 16.6$ mrad. In simulation only processes included in GEANT are taken into account. Normalization corresponds to the number of initial photons $1.5 \cdot 10^8$.

Fig. 10. Distributions of photons, detected in the range of angles $2.6 \div 16.6$ mrad for empty-target runs, over the parameter $(E_C - E_{TS})/\sigma_e$. (a) Experimental data (circles) and simulation (histogram, processes included in GEANT are only taken into account). (b) Contributions of different effects to the histogram (a): Compton scattering (solid line), secondary photons from showers (dashed line), photons passed the target and absorber without interaction (dotted line). Normalization corresponds to the number of initial photons 10^9 .

Fig. 11. Distributions of photons, detected in the range of angles $2.6 \div 16.6$ mrad for runs with target, over the parameter $(E_C - E_{TS})/\sigma_e$. (a) Experimental data (circles) and simulation with the use of GEANT package (histogram) including Delbrück scattering, photon splitting, and the background from the BGO-collimator. (b) Experimental data (circles), simulation (solid line), Delbrück scattering (dashed line), and the sum of all background processes (dotted line). Normalization corresponds to the number of initial photons 10^9 .

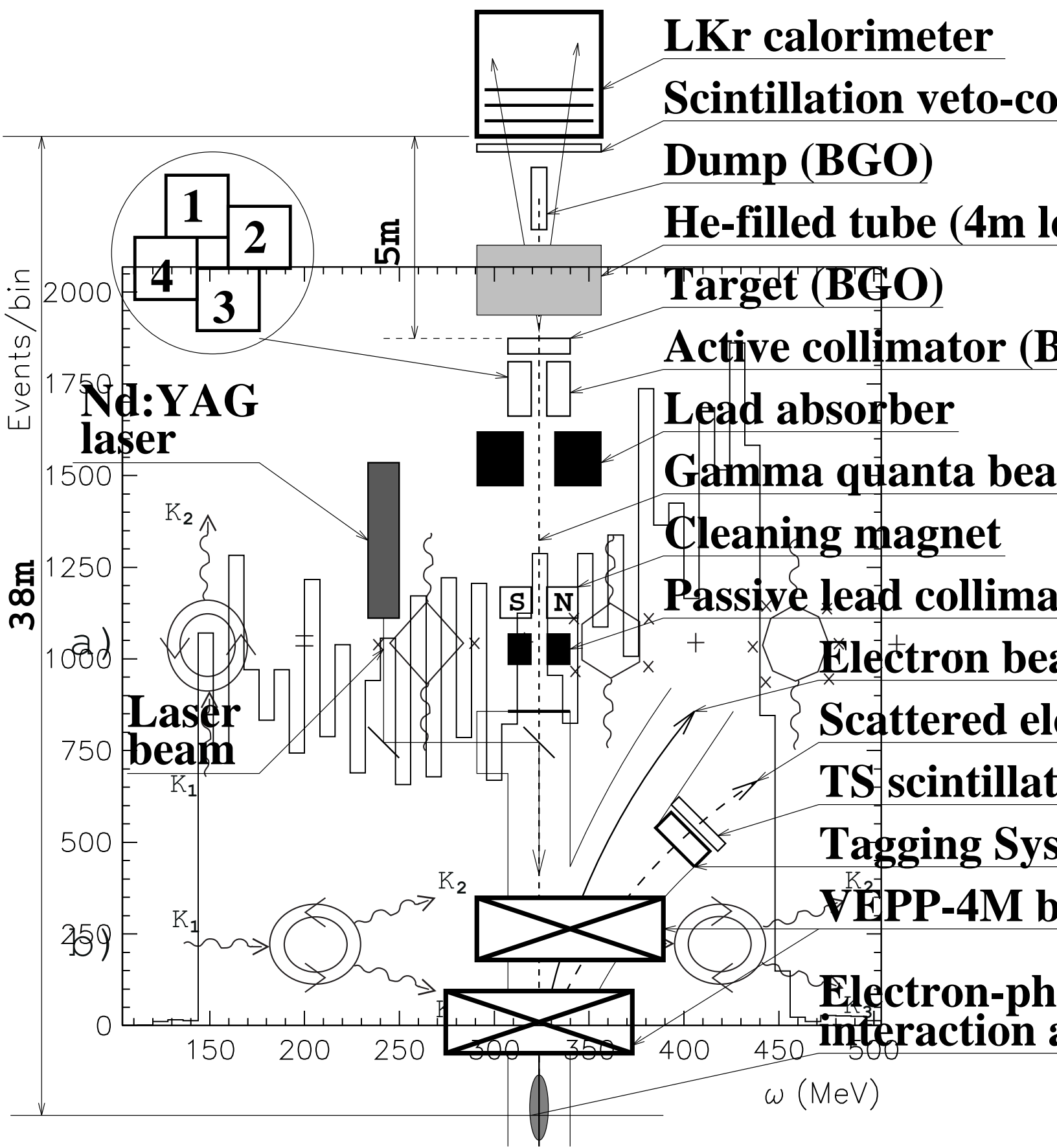
Fig. 12. The differential cross section of photon scattering $d\sigma/dt$ as a function of the momentum transfer Δ for a molecule of bismuth germanate. (a) Experimental data (circles) and background (squares). (b) Experimental data after subtraction of background (circles). Solid line is the result of calculation.

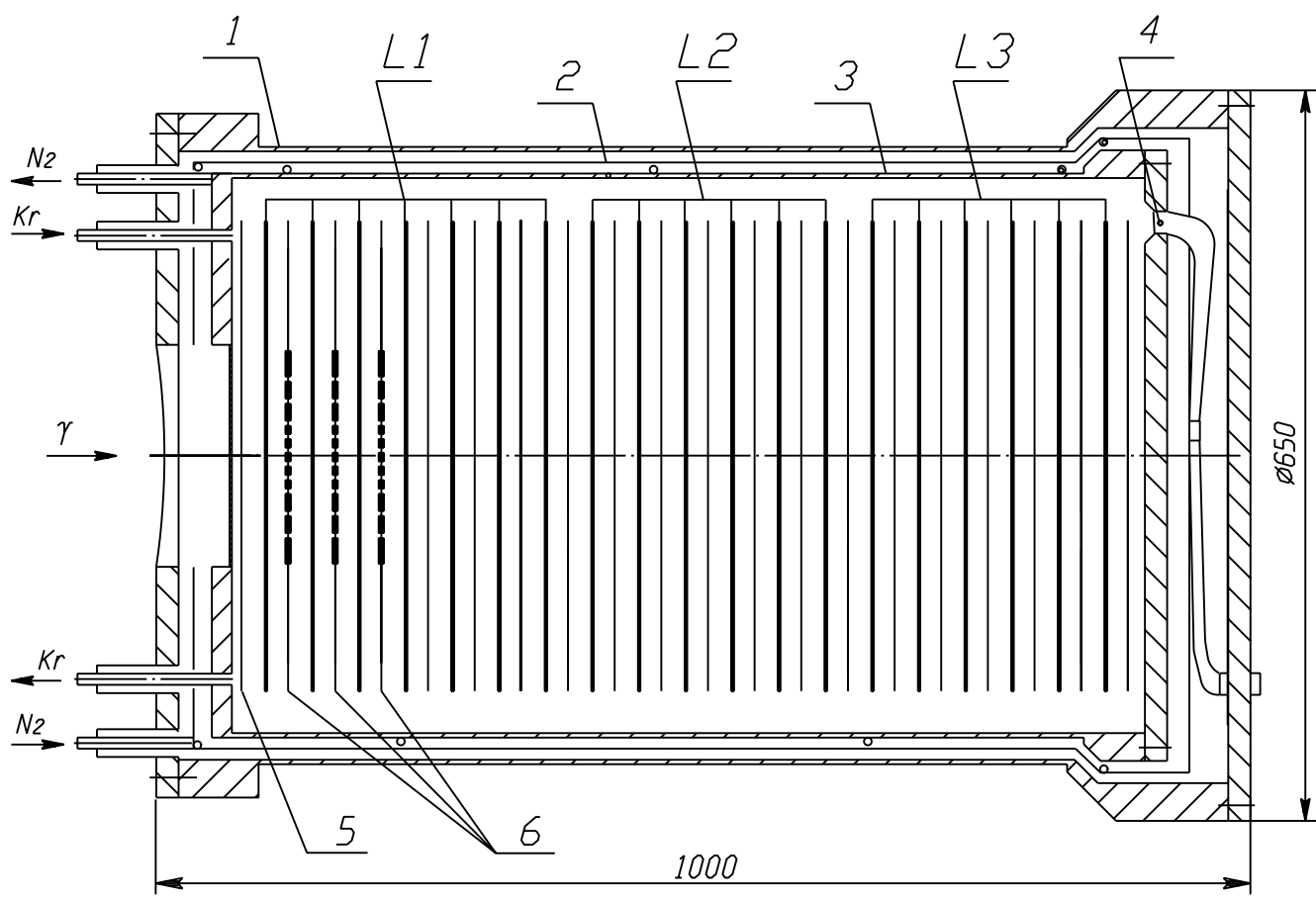
TABLE I. Number of photons, detected in the range of angles $2.6 \div 16.6$ mrad at $\Delta E < 2.5\sigma_c$. Data in each column are normalized to the number of initial photons 10^9 .

ω , MeV	$140 \div 450$	$140 \div 250$	$250 \div 350$	$350 \div 450$
Number of initial photons	$902.2 \cdot 10^6$	$275.4 \cdot 10^6$	$259.9 \cdot 10^6$	$366.9 \cdot 10^6$
Experiment	13172 ± 232	16810 ± 353	13252 ± 301	10383 ± 229
Simulation	12810 ± 181	16709 ± 329	12535 ± 283	10079 ± 209
Delbrück scattering	9120 ± 111	12346 ± 171	8884 ± 150	6867 ± 119
Compton scattering	1334 ± 45	1624 ± 85	1254 ± 80	1173 ± 66
Secondary photons	52 ± 8	60 ± 16	57 ± 16	42 ± 13
Photons passed without interaction	495 ± 62	954 ± 133	324 ± 65	270 ± 51
Photon splitting	435 ± 88	434 ± 90	519 ± 108	376 ± 78
Background from the BGO-collimator	1374 ± 124	1290 ± 246	1497 ± 214	1351 ± 147

Table II. The differential cross section of Delbrück scattering $d\sigma/dt$ for a molecule of bismuth germanate.

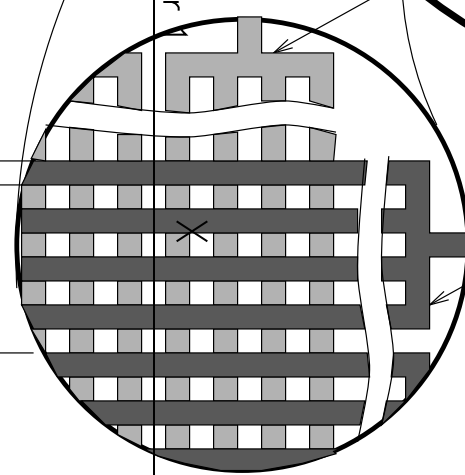
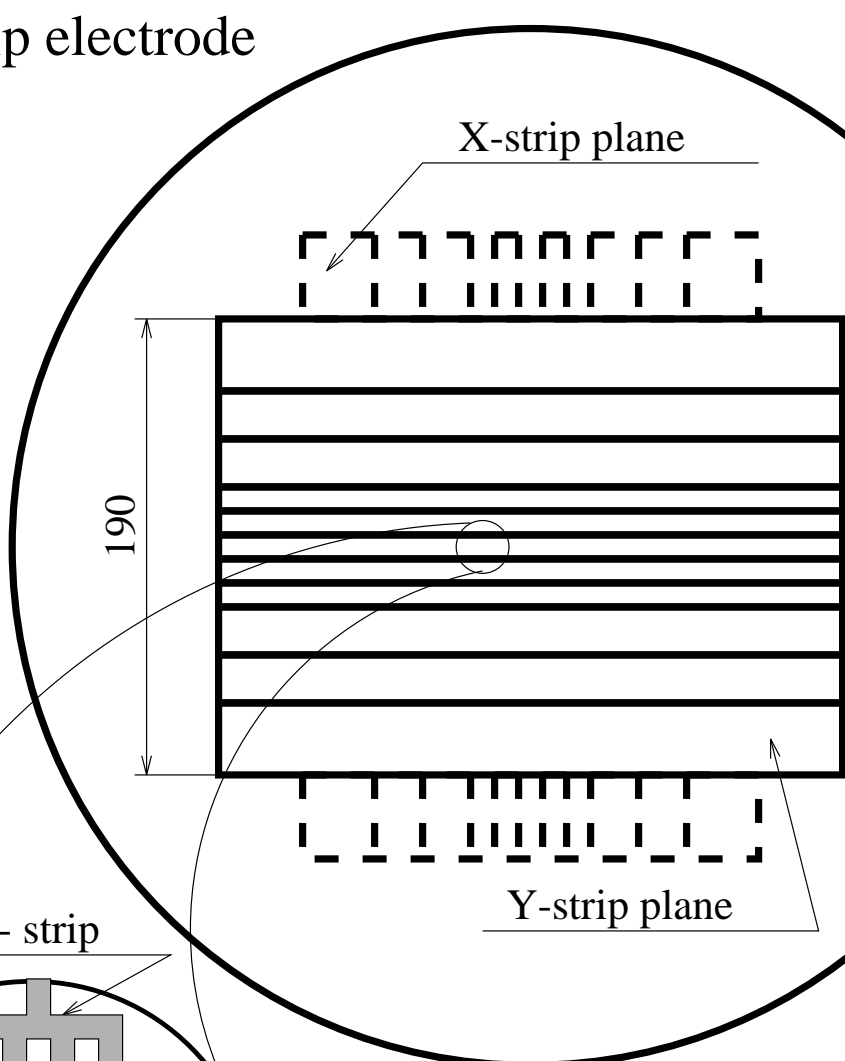
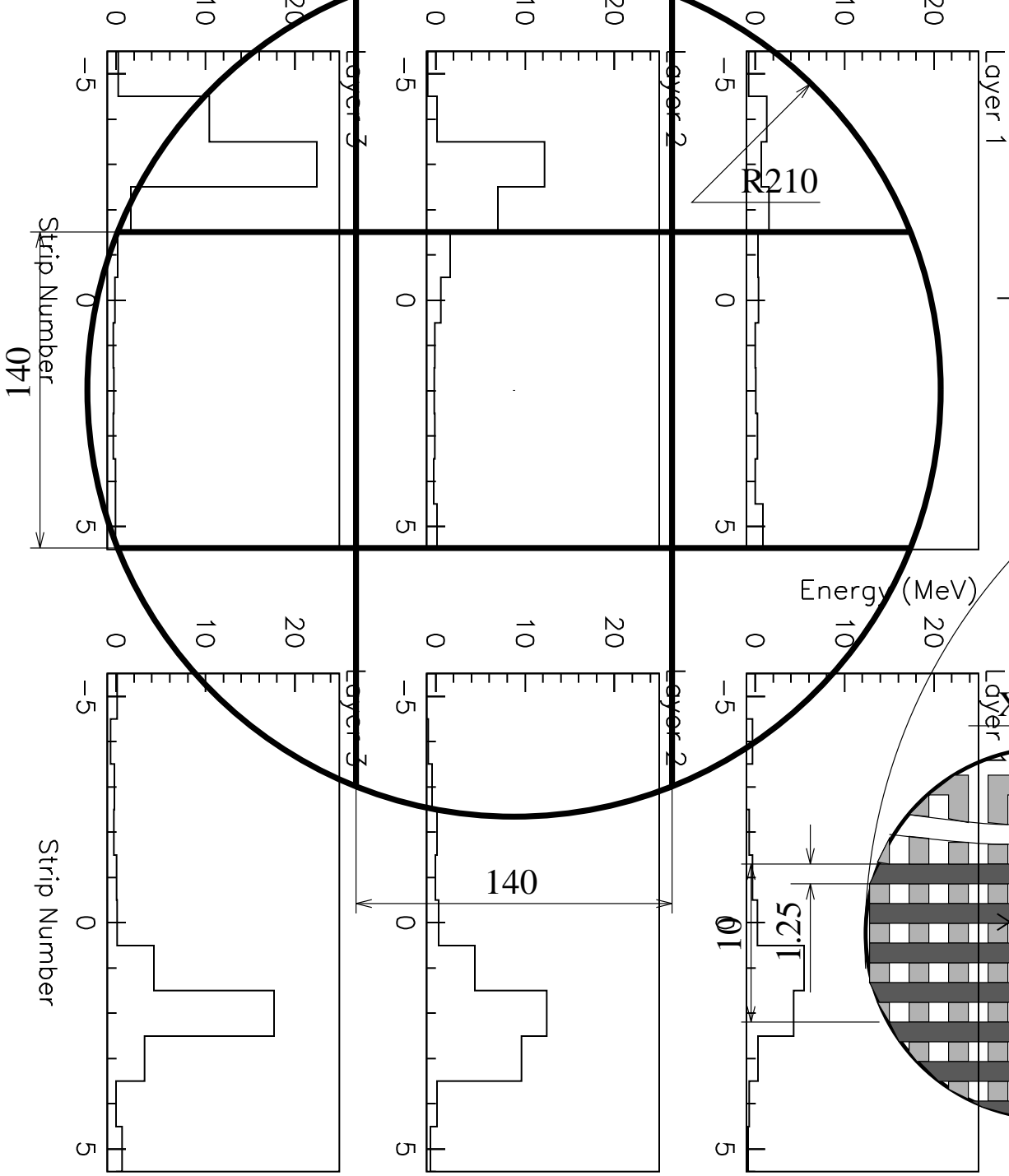
Δ (MeV)	$\frac{d\sigma}{dt}$ (mb/MeV ²), Calculation	$\frac{d\sigma}{dt}$ (mb/MeV ²), Experiment
0.49	21.1	19.9 ± 3.4
0.62	12.9	10.1 ± 1.2
0.75	8.30	8.10 ± 0.62
0.88	5.55	5.25 ± 0.36
1.01	3.83	3.88 ± 0.25
1.14	2.72	3.07 ± 0.18
1.27	1.99	2.09 ± 0.13
1.40	1.49	1.66 ± 0.11
1.53	1.13	1.12 ± 0.08
1.66	0.883	0.966 ± 0.073
1.79	0.696	0.758 ± 0.064
1.92	0.555	0.569 ± 0.059
2.05	0.450	0.476 ± 0.056
2.18	0.369	0.410 ± 0.055
2.31	0.306	0.356 ± 0.045
2.44	0.255	0.238 ± 0.049
2.57	0.215	0.148 ± 0.038
2.70	0.183	0.139 ± 0.035
2.83	0.157	0.187 ± 0.035
2.96	0.135	0.151 ± 0.028
3.09	0.116	0.112 ± 0.030
3.22	0.101	$(9.65 \pm 2.7) \cdot 10^{-2}$
3.35	$8.85 \cdot 10^{-2}$	0.111 ± 0.029
3.48	$7.76 \cdot 10^{-2}$	$(9.0 \pm 2.6) \cdot 10^{-2}$
3.61	$6.83 \cdot 10^{-2}$	$(7.0 \pm 2.3) \cdot 10^{-2}$
3.74	$6.07 \cdot 10^{-2}$	$(6.7 \pm 2.2) \cdot 10^{-2}$
3.87	$5.37 \cdot 10^{-2}$	$(6.1 \pm 2.1) \cdot 10^{-2}$
4.00	$4.80 \cdot 10^{-2}$	$(7.1 \pm 2.0) \cdot 10^{-2}$
4.13	$4.28 \cdot 10^{-2}$	$(3.9 \pm 2.1) \cdot 10^{-2}$
4.26	$3.84 \cdot 10^{-2}$	$(3.0 \pm 1.9) \cdot 10^{-2}$
4.39	$3.46 \cdot 10^{-2}$	$(5.0 \pm 2.1) \cdot 10^{-2}$
4.52	$3.11 \cdot 10^{-2}$	$(3.1 \pm 1.9) \cdot 10^{-2}$
4.65	$2.82 \cdot 10^{-2}$	$(4.7 \pm 1.8) \cdot 10^{-2}$
4.78	$2.53 \cdot 10^{-2}$	$(5.3 \pm 1.7) \cdot 10^{-2}$
4.91	$2.32 \cdot 10^{-2}$	$(2.2 \pm 1.7) \cdot 10^{-2}$
5.04	$2.11 \cdot 10^{-2}$	$(3.2 \pm 1.7) \cdot 10^{-2}$

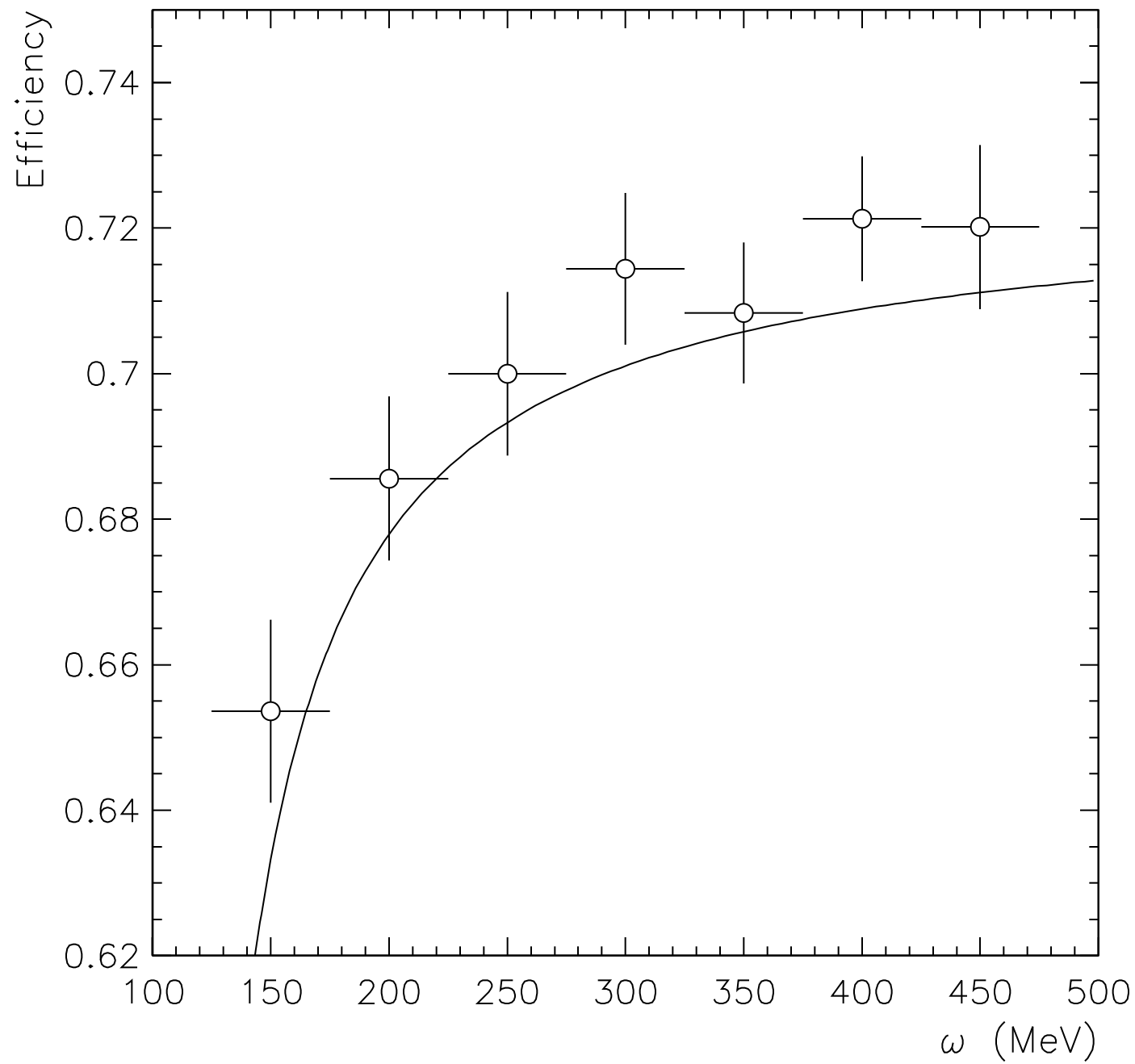


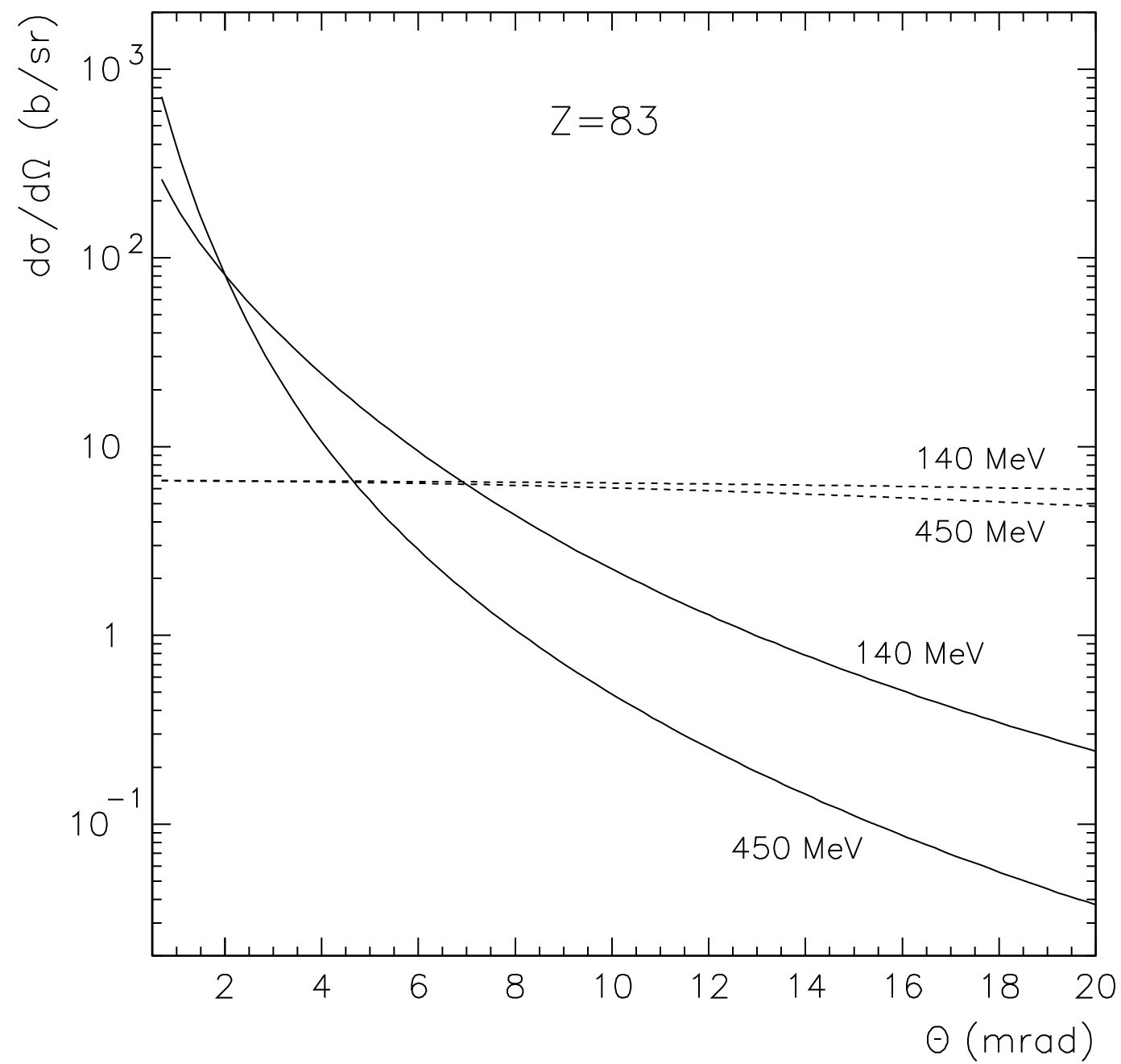


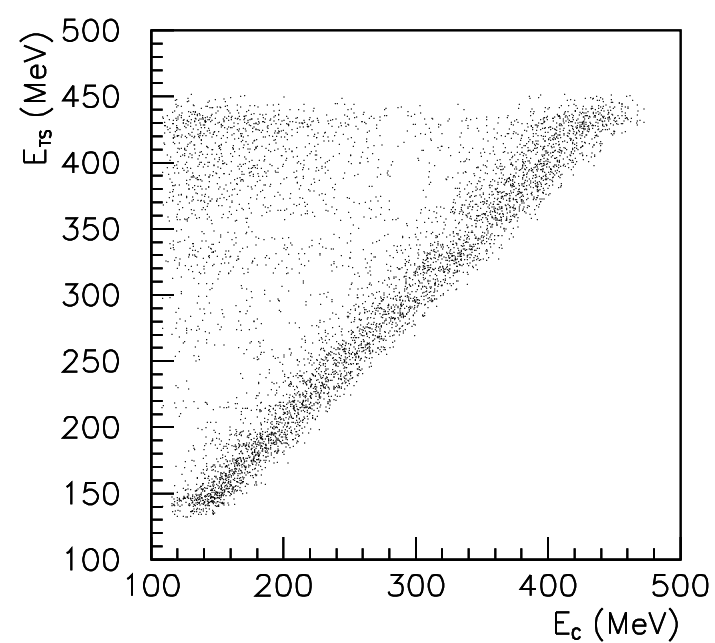
Tower electrode

Strip electrode

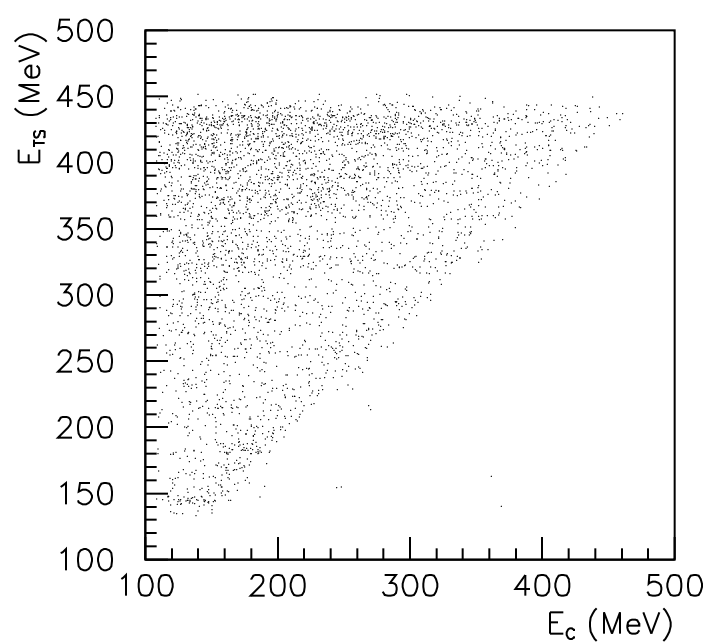




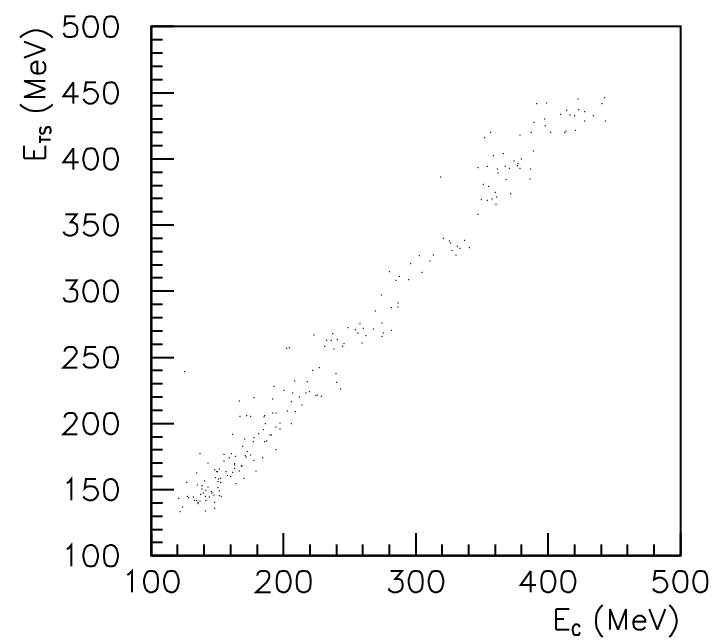




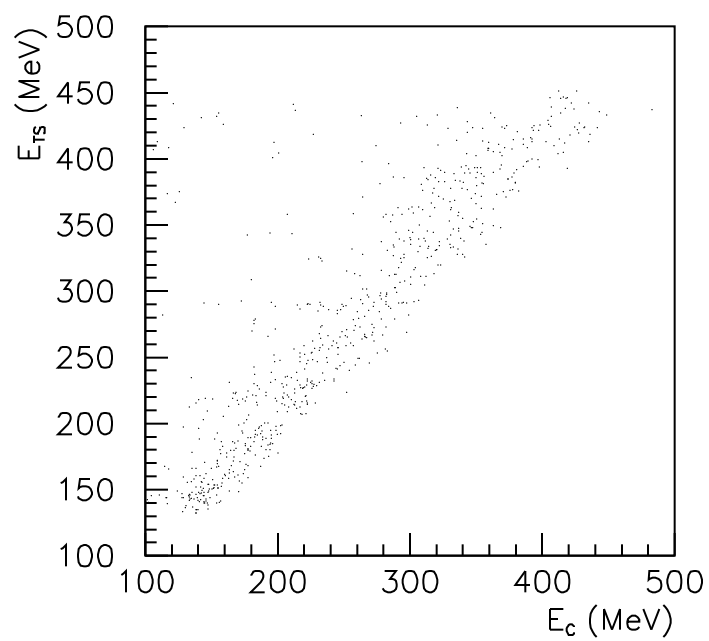
a) Experiment, with target



b) Experiment, no target



c) Simulation, with target



d) Simulation, no target

